Check for updates

Effect of substrate temperature on the microstructural and optical properties of chemical molecular beam deposited sb$_2$s$_3$ films

T. M. Razykov[1], K. M. Kuchkarov[1], M. S. Tivanov[2], L. S. Lyashenko[2], D. Z. Isakov[1,*], R. R. Khurramov[1], Z. Makhmudov[1], A. N. Olimov[1], M. Pirimmetov[1], P. A. Sivtsova[2], R. T. Yuldoshov[1], L. Schmidt-Mende[3], K. F. Shakhriev[1], Sh. B. Utamuradova[4], and J. G. Bekmirzoyev[1]

[1] *Physical-Technical Institute, Chingiz Aytmatov Str. 2B, 100084 Tashkent, Uzbekistan*

[2] *Faculty of Physics, Belarusian State University, Nezavisimosti Ave. 4, 220030 Minsk, Republic of Belarus*

[3] *Faculty of Physics Fach, University of Konstanz, Universitätsstr 10, 680D-78457 Constance, Germany*

[4] *Institute of Semiconductors Physics and Microelectronics, Yangi Olmazor Street 20, 100057 Tashkent, Uzbekistan*

ABSTRACT

In this work, Sb$_x$S$_y$ thin films were grown on glass substrates for the first time using the chemical molecular beam deposition method in the atmospheric pressure hydrogen flow. The structural, morphological and optical properties of Sb$_x$S$_y$ thin films grown at different substrate temperatures of 300 °C, 350 °C, 400 °C and 450 °C were studied. XRD results showed that the Sb$_x$S$_y$ thin films grown at different substrate temperatures have an orthorhombic crystal structure. Phase analysis indicated a weakening of Sb-S bonds with increasing substrate temperature. Also, the grain sizes of all obtained thin films ranged from 0.5 to 3 μm. The increase in temperature caused the grains to grow and the spaces between them to increase. Optical experiments reveal that as the substrate temperature increases, the optical band gap energy of the films increases from 1.52 eV to 1.73 eV, as well as an increase in the Urbach energy from 0.11 eV to 0.44 eV. The experimental values of the band gap for Sb$_2$S$_3$ films are near the optimum value for photovoltaic conversion.

1 Introduction

Metal chalcogenides, including CdTe, Cu(In,Ga)Se2 (CIGS) as well as MAPI perovskite thin films, have achieved relatively high efficiency as light harvesting materials due to their high absorption coefficients and excellent optoelectronic properties. However, the scarcity and high cost of Te, In, and Ga, and the toxicity of Cd and Pb elements may prevent long-term large-scale implementation of PV technologies [1–3]. Hence, scientists worldwide are researching new types of benign and abundant elements in the Earth's crust instead of these materials. Scientists are showing great interest in the elements antimony (Sb), selenium (Se), and sulfur (S) as materials that meet the aforementioned criteria.

🖄 Springer

Currently, a lot of research has been done on the thin film of Sb_2X_3 (X = Se,S), which is used as an absorbing in various studies. One of the main reasons for this is its competitive physical properties [4–8]. Sb_2X_3-thin films were grown by several methods (vapor transport deposition, close spaced sublimation, chemical bath deposition, sputtering and etc.) [9–13]. The primary goal of the ongoing research is to optimize the physical properties of Sb_2X_3 thin films and obtain a solar cell with high efficiency.The quality of the obtained films depends on their structural, morphological and optical properties. The crystal orientation of Sb_2S_3 thin films plays a crucial role in the performance of the solar cells as it provides valuable information about the charge carrier transport and the formation of useful grain boundaries [14]. A thin film of Sb_2X_3 can crystallize during growth in horizontal (hkl, $l = 0$) or vertical (hkl, $l \neq 0$) directions, depending on the type and temperature of the substrate. The vertical crystallization of Sb_2S_3 ribbons along the c-axis to the substrate is considered useful for the transport of charge carriers through the absorber film [14, 15].

Recently, we have discussed fabrication of Sb_xSe_y films by chemical molecular beam deposition (CMBD) method in the atmospheric pressure gas flow from Sb and Se precursors [16] and their characteristics [17].

Fabrication of thin films Sb_2S_3 by CMBD (Fig. 1) in the atmospheric pressure hydrogen flow and their characterizations are discussed in this paper.

2 Experiments

2.1 Synthesis of Sb_2S_3

The process involved utilizing semiconductor-grade granules of Sb_2S_3 (purity: 99.999%), sourced from Chemsavers (USA), as the initial material. These granules were then placed into containers, and the system was activated and purged with hydrogen to eliminate atmospheric polluting gases. Soda-lime glasses (SLG) were used as substrates. The SLG substrates underwent a cleaning process involving detergent, acetone, ethanol, and deionized water in an ultrasonic bath, followed by drying with a stream of N_2 gas. Consequently, the outer oven of the reaction chamber was activated. The heating level is determined by the set deposition temperatures, which are controlled by chromel–alumel thermocouples. When the substrate reached the required temperature level, individual
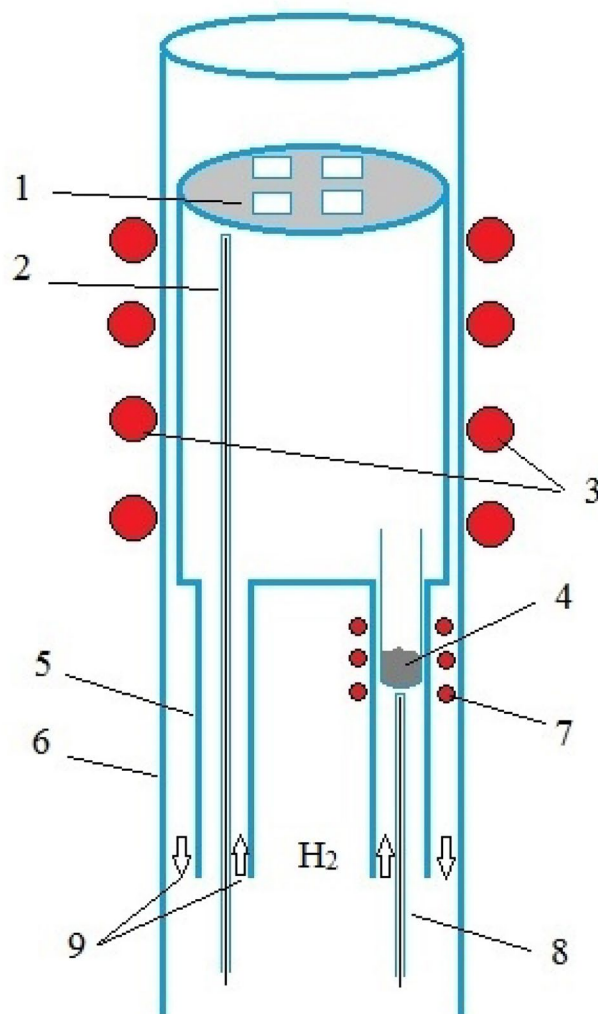

Fig. 1 Scheme of CMBD device. 1. Substate 2. Thermocouples 3. External heater 4. Source material 5. Reaction chamber 6. Reactor 7. Source heater 8. Thermocouples 9. Gas inlet and outlet

heating furnaces for the Sb_2S_3 binary compound were activated and brought to the required evaporation temperatures. The evaporation process for the Sb_2S_3 granules was carried out within the temperature range of 650–700 °C, while the substrate temperature ranged from 300 °C to 450 °C. The hydrogen carrier gas flow was ~ 20 cm^3/min.

At the Sb_2S_3 evaporation temperatures of 650–700 °C, granules transfer into the vapour phase and dissociates to Sb and S_2:

$$2SbS(s) + H_2 \rightarrow 2Sb(g) + S_2(g) + H_2 \tag{1}$$
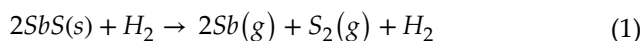
S_2 (g) reacts with hydrogen, and hydrogen sulfide is formed [18]:

$$S_2(g) + 2H_2 \rightarrow 2H_2S(g) \tag{2}$$

Sb and S atoms and H_2S molecules cover the surface of the substrate, and Sb_2S_3 films are formed as a consequence of their interaction:

$$2Sb(g) + S_2(g) + H_2S(g) \rightarrow Sb_2S_3(s) + H_2 \tag{3}$$
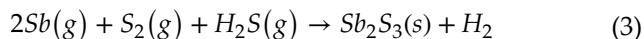
The deposition process was carried out for 30 minutes. Four samples were used for each experiment, and the dimensions of the samples were 2.0×2.0 cm^2. The deposited samples were replicated 5 times (20 samples) at each substrate temperature. The morphological characteristics (average grain size), structural features (main crystallographic growth orientations), and optoelectronic properties (band gap, Urbach energy) of the samples within each group exhibited nearly indistinguishable similarities. In this way, high-quality Sb_2S_3 films were obtained at various substrate temperatures.

2.2 Films characterization

The elemental (chemical) composition of the synthesized Sb_2S_3 films was determined by X-ray spectral microanalysis (XMA) using an energy-dispersive nitrogen-free spectrometer Aztec Energy Advanced X-Max 80. Surface morphology features were examined using scanning electron microscopy (SEM) with an electron microscope LEO1455VP in secondary electrons mode. Surface topography analysis was conducted using a SOLVER NANO atomic force microscope (AFM), employing semi-contact mode scanning with a probe featuring a tip radius of 10 nm at a resonant frequency of 178 kHz.

Using a high-resolution diffractometer Rigaku Ultima IV in the geometry of a sliding beam, diffraction patterns were captured within the angle range $2\theta = 10–60°$ using CuKα radiation with a wavelength of 0.15418 nm. Raman spectra were measured at room temperature on a Nanofinder HE confocal spectrometer (LOTIS TII). A solid-state laser with a wavelength of 532 nm was used; laser radiation with a power of 60 μW was focused on the surface of the samples into an area with a diameter of about 0.7 μm. The signal accumulation time was 30–60 s. The spectral resolution was no worse than 2.5 см$^{-1}$. Specular optical reflection and transmission spectra were recorded with a spectral resolution of no worse than 5 nm in the wavelength range 400 ÷ 3000 nm in unpolarized light using a Photon RT multifunctional scanning spectrophotometer (EssentOptics). The optical radiation beam size on the sample surface measured approximately 2×6 mm^2.

The thickness of the deposited films was determined using micro weighing on an FA 120 4C balance (with an accuracy of 0.1 mg) and was about ~ 2 μm.

3 Results and discussion

Figure 2 shows XRD images of Sb_2S_3 thin films grown at various substrate temperatures (300 °C, 350 °C, 400 °C and 450 °C). At all substrate temperatures (except 450 °C), the XRD analysis revealed distinct peaks corresponding to horizontal growth directions such as (020), (120), (130), (240), and (211), (221), (301) which is favorable for solar cells [19, 20] indicating its orthorhombic structure as per JCPDS pdf 00–006-0474. Additionally, peaks corresponding to Sb were observed at (012), (104), and (110) planes in the Sb_2S_3 thin films, consistent with JCPDS pdf 01–085-1322, across all substrate temperatures. Notably, at the highest substrate temperature of 450 °C, the intensity of Sb_2S_3 peaks notably diminished, particularly (020), (120), (130), (211), (221), and (501). While the intensity of peaks corresponding to Sb, such as (012), (110) and (202), remained with notable portion between 400 °C and 450 °C. This observation suggests that excessively high substrate temperatures are unfavorable for Sb_2S_3 thin film formation. The consistent presence of Sb peaks in all samples indicates a high proportion of Sb
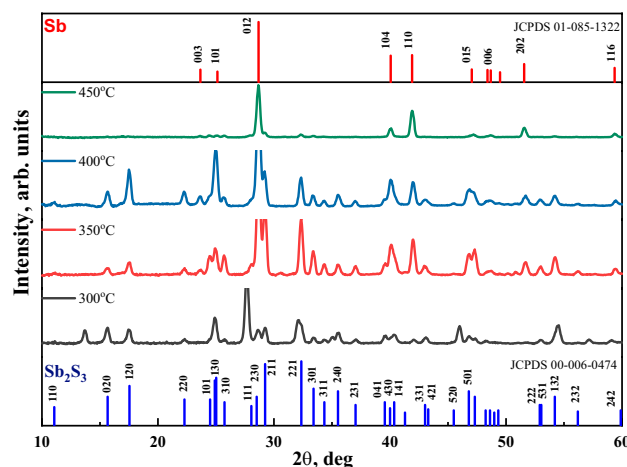

Fig. 2 XRD patterns of Sb_xS_y thin films at different substrate temperatures

within the Sb_2S_3 thin film composition. Peaks such as (211) and (221), which exhibit better electrophysical properties in thin layers, reached a maximum value at a substrate temperature of 350 °C, and the intensity of these peaks showed relatively low values at other substrate temperatures.

For Sb_xS_y thin films, phase analysis was carried out in order to check the bonding of Sb with S. (Fig. 3). Raman spectroscopy analysis showed that intensity peaks at 110 cm^{-1}, 150 cm^{-1}, 237 cm^{-1}, 280 cm^{-1}, and 310 cm^{-1} are present in all Sb_2S_3 thin films. This confirms that the main lattice structure is preserved in the grown samples. It can be seen from the figure that the intensity of the 280 cm^{-1} and 310 cm^{-1} peaks increases with the decrease of the substrate temperature. These peak values correspond to Sb-S vibration phases [21]. The intense peak at 237 cm^{-1} is almost unchanged with the change of the substrate temperature. The band at 237 cm^{-1} corresponds to symmetric S-Sb-S bending
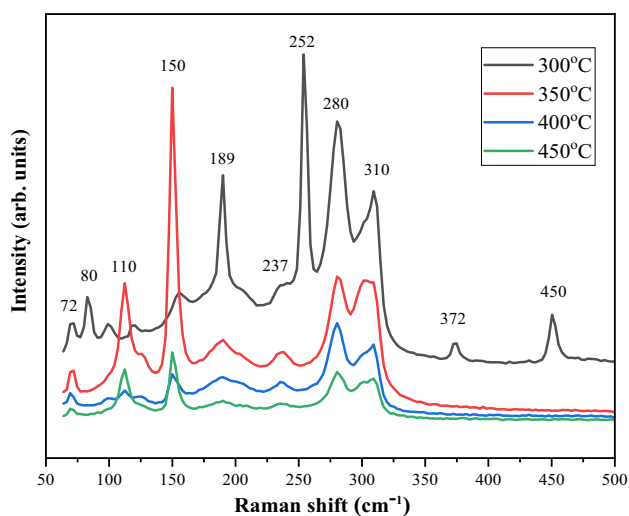
modes [22, 23]. Intense peaks at 110 cm^{-1} and 150 cm^{-1} indicate the presence of Sb-Sb phases in thin films [24]. In addition, there are several intense peaks at 80, 189, 372, 252, and 450 cm^{-1} in Sb_2S_3 thin films, and these peaks correspond to Sb_2O_3 phases [25]. It can be seen that peaks at 80, 252, 372 and 450 cm^{-1}, which were not detected in the other films, appeared at the substrate temperature of T_{sub} = 300 °C. The intensity of 72 cm^{-1} peak, corresponding to the Sb_2O_4 phase [26], decreased with the increase of substrate temperature.

Morphological properties of Sb_xS_y thin films grown by CMBD method were studied using scanning electron microscopy (SEM) and atomic force microscopy (AFM) (Figs. 4 and 5). SEM micrographs (Fig. 4) show that Sb_xS_y thin films have a microcrystalline structure, which appearance depends on the substrate temperature. Sb_xS_y thin films prepared at substrate temperatures of 300 °C and 350 °C have a much smoother surface. Sb_xS_y films are cylindrical in shape with a length of 1–2 μm and a diameter of 500 nm. Some of the grains coalesced to form 2–3 μm large grains. Such associations were also observed in samples obtained by the vapor transport deposition (VTD) method [27]. The most uniform structure with a crystallite size of about 1 μm have films, grown with a substrate temperature of 350 oC. The crystallites have a columnar, close to cylindrical shape. An increasing of the substrate temperature leads to the appearance of some large crystallites, which quantity and size increase with increasing the substrate temperature [28]. At a temperature of 450 °C, the crystallite maximum size reached 3 microns, the gaps between them have grown significantly. At the same time, as the substrate temperature increased, the proportion of crystallites with minimal dimensions decreased (Table 1).

As can be seen from the table, at a temperature of 350 °C, the asymmetry and kurtosis reach maximum values, which correlates with a change in
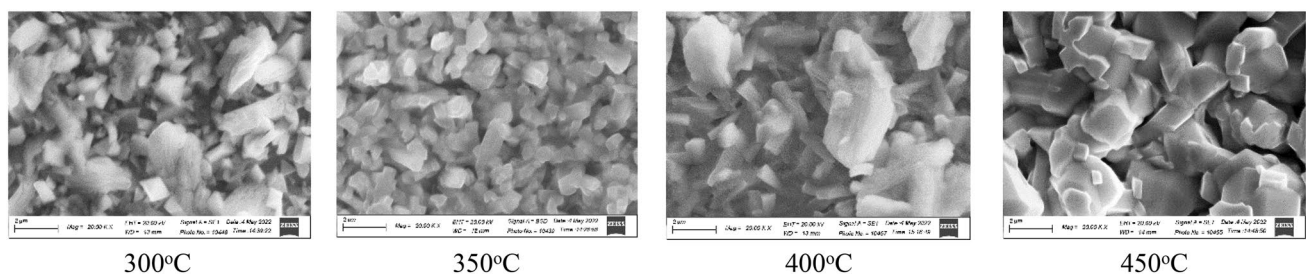

Fig. 3 Raman spectra of Sb_xS_y thin films at different substrate temperatures

Fig. 4 Surface morphology of Sb_xS_y thin films at different substrate temperatures
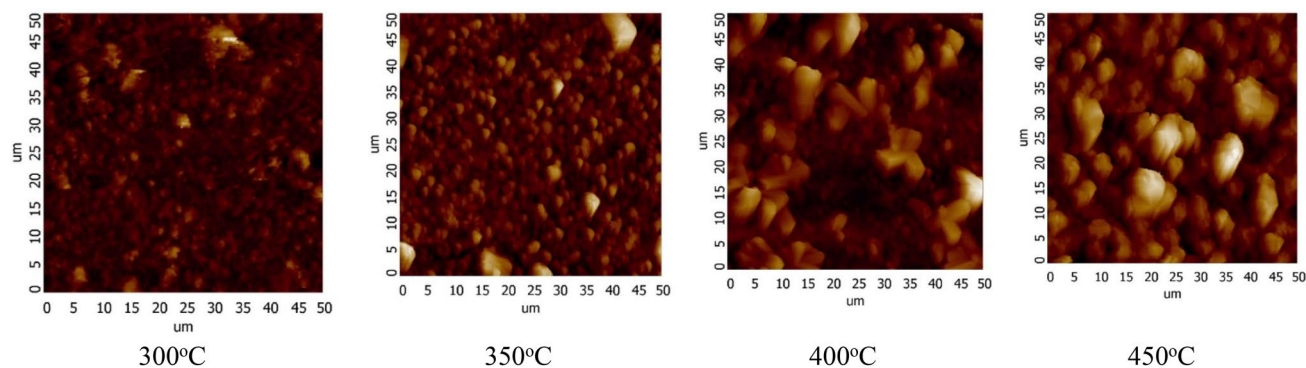
Fig. 5 2D topography obtained on an AFM of the surface of Sb_xS_y thin films at different substrate temperatures

Table 1 Surface roughness parameters of Sb_xS_y thin films at different substrate temperatures

T_{sub}, ºC	300	350	400	450
Average roughness Sa, µm	0.25	0.32	0.73	0.77
RMS roughness Sq, µm	0.32	0.42	0.91	0.97
Skewness Ssk	0.86	0.91	0.74	0.52
Kurtosis Sku	4.37	4.82	3.25	3.20

the morphology of the surface shown in the SEM images. At a temperature of 350 °C, the surface with the largest number of peaks is formed. However, for all films have Sku > 3, which indicates the formation at all substrate temperatures the surfaces with a lot of peaks.

Optical transmission (T) and reflection (R) spectra of Sb_2S_3 films deposited at T_{sub} = 350 °C and T_{sub} = 400 °C shown in Fig. 6. Using the optical transmission and reflection data, the absorption coefficient (α) of the films was determined by the following equation:

$$\alpha = -\frac{1}{d} \ln \left(\frac{\sqrt{(1-R)^4 + 4T^2R^2} - (1-R)^2}{2TR^2} \right), \quad (4)$$

where d is the thickness of the films. Thickness of the films were around 2 µm.

For a direct- allowed transitions, bandgap of Sb_2S_3 thin films can be determined by extracting the Tauc fitting, as shown in Fig. 6(c):

$$(\alpha h\nu)^2 = A\left(h\nu - E_g\right), \quad (5)$$

where hν is the incident photon energy and A is a constant. The band gap ranged from 1.52 to 1.73 eV

depending on the substrate temperature. The optical band gap energy of Sb_2S_3 thin films increases as the substrate temperature increases, which may be attributed to the difference in morphology and crystallinity of the obtained samples [29, 30]. The obtained band gap values indicate that the synthesized Sb_2S_3 films may be very promising for applications in solar energy and optoelectronics [31].

To study the structural disorder of Sb_xS_y films, the Urbach energy (E_U) was also calculated. The value of E_U indicates the level of crystallinity and structural defects present in the films. In the low photon energy range, an exponential variation in the absorption edge followed the Urbach empirical equation:

$$\alpha = \alpha_0 \exp \left[\frac{h\nu}{E_U} \right], \quad (6)$$

where α_0 is a constant. The value of E_U can be obtained from the inverse slope of the linear plot of $\ln(\alpha)$ vs hν as shown in Fig. 6d. The values of the Urbach E_U energy increase from 0.11 eV to 0.44 eV as the substrate temperature increases. A low E_U value indicates a sufficiently low defect rate of the films.

4 Conclusion

The effect of substrate temperature on the structural, morphological, and optical properties of Sb_xS_y thin films grown by the CMBD method was studied. The XRD analysis revealed an orthorhombic crystal structure for the films grown at different substrate temperatures. At a substrate temperature of 350 °C, the peaks of the preferred orientations (211) and (221) showed better value than other samples. Raman spectroscopy confirmed the preservation of the main
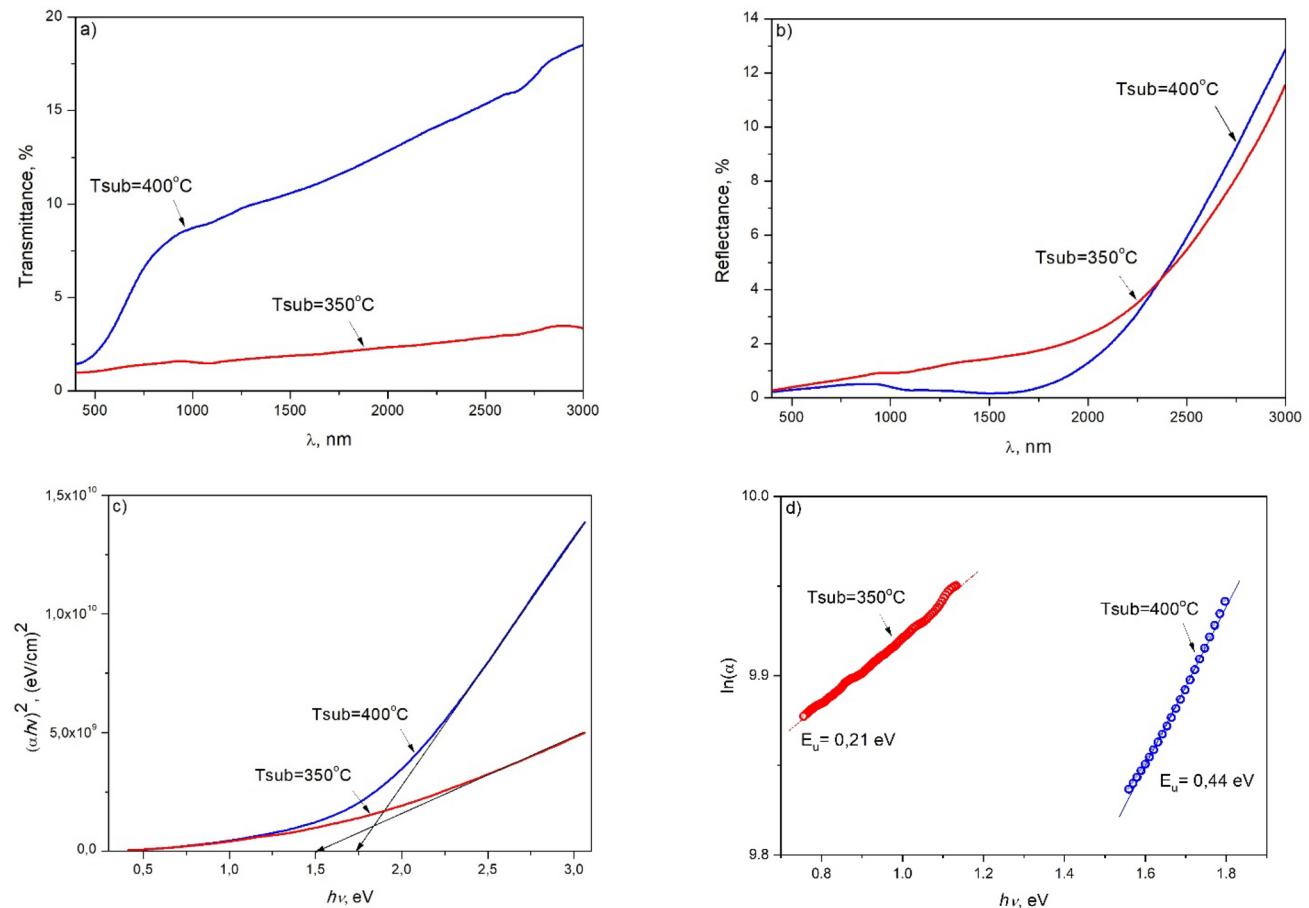
Fig. 6 a Transmission and **b** Reflectance spectra, **c** Plots of function $(\alpha h\nu)^2 = f(h\nu)$ for Sb_xS_y films obtained at $T_{sub} = 350$ °C ($E_g = 1.52$ eV) and $T_{sub} = 400$ °C ($E_g = 1.73$ eV), **d** Plots of function $\ln(\alpha) = f(h\nu)$ for Sb_xS_y films

lattice structure across all samples, with variations in peak intensities attributed to Sb-S vibration phases and symmetric S-Sb-S bending modes. The weakening of Sb-S bonds with increasing substrate temperature was observed. SEM and AFM analysis provided insights into the morphological properties, revealing changes in grain size and surface roughness with increasing substrate temperature. The surfaces of thin films obtained at the substrate temperature of 350 °C were compact and had the best uniformity. Additionally, optical characterization indicated an increase in the band gap energy with increasing temperature. Overall, these findings contribute to our understanding of the growth parameters influencing the properties of Sb_xS_y thin films and provide valuable insights for optimizing their performance in various applications.

Author contributions

Sharifa Utamuradova, Javoxir Bermirzoyev. Supervision: Takhir Razykov. All authors read and approved the final manuscript.

Data availability

The data used in the current study are available from the corresponding author on reasonable request.

Declarations

Conflict of interest   There are no conflicts of interest to disclose between the authors.

References

1. T.D. Lee, A.U. Ebong, A review of thin film solar cell technologies and challenges. Renew. Sustain. Energy Rev. **70**, 1286–1297 (2017). https://doi.org/10.1016/j.rser.2016.12.028

2. K. Zeng, D.-J. Xue, J. Tang, Antimony selenide thin-film solar cells. Semicond. Sci. Technol. **31**, 063001 (2016)

3. N. Mufti, T. Amrillah, A. Taufiq, M. AriprihartaSunaryono, Z. Diantoro, H. Nur, Review of CIGS-based solar cells manufacturing by structural engineering. Sol. Energy **207**, 1146–1157 (2020). https://doi.org/10.1016/j.solener.2020.07.065

4. N. Juneja, S. Daskeviciute-Geguziene, N. Spalatu, Employment of dopant-free fluorene-based enamines as innovative hole transport materials to boost the transparency and performance of Sb_2S_3 based solar cells. Mater. Sci. Semicond. Process.Semicond. Process. **169**, 107934 (2024). https://doi.org/10.1016/j.mssp.2023.107934

5. C. Lan, J. Luo, H. Lan, B. Fan, H. Peng, J. Zhao, H. Sun, Z. Zheng, G. Liang, P. Fan, Enhanced charge extraction of Li-doped TiO_2 for efficient thermalevaporated Sb_2S_3 thin film solar cells. Materials **11**(3), 355 (2018). https://doi.org/10.3390/ma11030355

6. Y.C. Choi, D.U. Lee, J.H. Noh, E.K. Kim, S.I. Seok, Highly improved Sb_2S_3 sensitized-inorganiceorganic heterojunction solar cells and quantification of traps by deep-level transient spectroscopy. Adv. Funct. Mater. (2014). https://doi.org/10.1002/adfm.201304238

7. J.A. Christians, P.V. Kamat, Trap and transfer. Two-step hole injection across the Sb2S3/CuSCN interface in solid-state solar cells. ACS Nano **7**, 7967–7974 (2013). https://doi.org/10.1021/nn403058f

8. Y. Yin, C. Wu, R. Tang, C. Jiang, G. Jiang, W. Liu, T. Chen, C. Zhu, Composition engineering of Sb_2S_3 film enabling high performance solar cells. Sci. Bull. **64**, 136–141 (2019). https://doi.org/10.1016/j.scib.2018.12.013

9. F. Aousgi, W. Dimassi, B. Bessais, M. Kanzari, Appl. Surface Sci. **350**, 19–24 (2015). https://doi.org/10.1016/j.apsusc.2015.01.126

10. A.D. Sindi, P.T. Shalvey, J.D. Major, Comparison of one and two-stage growth approaches for close space sublimation deposition of Sb_2Se_3 thin film solar cells. Mat. Sci. in Sem. Processing **174**, 108161 (2024). https://doi.org/10.1016/j.mssp.2024.108161

11 J. Escorcia-García, M. Domínguez-Díaz, A. Hernández-Granados, H. Martínez, MRS Adv. Mater. Res. Soc. (2018). https://doi.org/10.1557/adv.2018.551

12 X. Chena, Z. Li, H. Zhu, Y. Wang, B. Liang, J. Chen, X. Ying, Y. Mai, J. Mater. Chem. C (2017). https://doi.org/10.1039/c7tc02460f

13 M.I. Medina-Montes, Z. Montiel-Gonza ´lez, F. Paraguay-Delgado, N.R. Mathews, X. Mathew, J. Mater. Sci. Mater. Electron. **27**, 9710–9719 (2016). https://doi.org/10.1007/s10854-016-5033-0

14. X. Wen et al., Nat. Commun.Commun. **9**(1), 1–10 (2018)

15. H. Koc, A.M. Mamedov, E. Deligoz, H. Ozisik, First principles prediction of the elastic, electronic, and optical properties of Sb_2S_3 and Sb_2Se_3 compounds. Sol. State Sci. **14**, 1211 (2012). https://doi.org/10.1016/j.solidstatesciences.2012.06.003

16. T.M. Razykov, J. Bekmirzoev, A. Bosio, B.A. Ergashev, D. Isakov, R. Khurramov, K.M. Kouchkarov, M.A. Makhmudov, A. Romeo, N. Romeo, M.S. Tivanov, Sh.B. Utamuradova, D.S. Bayko, L.S. Lyashenko, O.V. Korolik, A.A. Mavlonov, Structural and optical properties of Sb_xSe_y thin films obtained by chemical molecular beam deposition method from Sb and Se precursors. Sol. Energy **254**, 67–72 (2023). https://doi.org/10.1016/j.solener.2023.03.010

17. K.M. Kuchkarov, T.M. Razykov, M.S. Tivanov, D.S. Bayko, L.S. Lyashenko, B.A. Ergashev, A. Mavlonov, A.N. Olimov, R. Khurramov, D.Z. Isakov, M. Pirimmatov,

Characteristics of thin Sb2Se3 films obtained by the chemical molecular beam deposition method for thin-film solar cells. Thin Solid Films **774**, 139844 (2023). https://doi.org/10.1016/j.tsf.2023.139844

18. B. de Darwent, R. Roberts, The photochemical and thermal decompositions of hydrogen sulphide. Proc. R. Soc. Lond. A **216**, 344–361 (1953). https://doi.org/10.1098/rspa.1953.0026

19. L.Q. Yao, L.M. Lin, Z.P. Huang, Y. Mao, H. Li, W.W. Lin, G.L. Chen, A liquid medium annealing strategy for highly [041]/[141]-oriented planar antimony sulfide solar cells with 7.23% efficiency. Nano Energy **106**, 108064 (2023)

20. U.A. Shah, S. Chen, G.M.G. Khalaf, Z. Jin, H. Song, Wide bandgap Sb2S3 solar cells. Adv. Func. Mater.Func. Mater. **31**(27), 2100265 (2021)

21. C.J. Diliegros-Godines, J.S. Cruz, N.R. Mathews, M. Pal, Effect of Ag doping on structural, optical and electrical properties of antimony sulfide thin films. J. Mater. Sci. **53**(16), 11562–11573 (2018). https://doi.org/10.1007/s10853-018-2420-3

22. R. Parize, T. Cossuet, O. Chaix-Pluchery, H. Roussel, E. Appert, V. Consonni, Mater. Des. **121**, 1–10 (2017)

23. S. Kharbish, E. Libowitzky, A. Beran, Raman spectra of isolated and interconnected pyramidal XS_3 groups (X = Sb, Bi) in stibnite, bismuthinite, kermesite, stephanite and bournonite. Eur. J. Mineral. **21**(2), 325–333 (2009). https://doi.org/10.1127/0935-1221/2009/0021-1914

24. X. Wang, K. Kunc, I. Loa, U. Schwarz, K. Syassen, Effect of pressure on the raman modes of antimony. Phys. Rev. B **74**, 134305 (2006). https://doi.org/10.1103/PhysRevB.74.134305

25. A. Shongalova et al., On the identification of Sb_2Se_3 using raman scattering. MRS Commun. **8**(3), 865–870 (2018). https://doi.org/10.1557/mrc.2018.94

26. G. Mestl, P. Ruiz, B. Delmon, H. Knozinger, Sb_2O_3/Sb_2O_4 in reducing/ oxidizing environments: an in situ Raman spectroscopy study. J. Phys. Chem. **98**, 11276–11282 (1994). https://doi.org/10.1021/j100095a008

27. P.V. Athma, A.I. Martinez, N. Johns, T.A. Safeera, R. Reshmi, E.I. Anila, Nanostructured zinc oxide thin film by simple vapor transport deposition. Superlattice. Microst. **85**, 379–384 (2015). https://doi.org/10.1016/j.spmi.2015.06.005

28. R. Suriakarthick, V.N. Kumar, T.S. Shyju, R. Gopalakrishnan, Effect of substrate temperature on copper antimony sulphide thin films from thermal evaporation. J. Alloy. Compd. **651**, 423–433 (2015)

29. Y. Yu, R. Wang, Q. Chen, L.-M. Peng, High-quality ultra-long Sb_2Se_3 and Sb_2S_3 nanoribbons on a large scale via a simple chemical route. J. Phys. Chem. B **110**, 13415–13419 (2006). https://doi.org/10.1021/jp061599d

30. H. Hu, M. Mo, B. Yang, X. Zhang, Q. Li, W. Yu, Y. Qian, Solvothermal synthesis of Sb2S3 nanowires on a large scale. J. Cryst. GrowthCryst. Growth **258**, 106–112 (2003). https://doi.org/10.1016/S0022-0248(03)01494-5

31. K. Li, Y. Xie, B. Zhou, X. Li, F. Gao, X. Xiong, B. Li, G. Zeng, M. Ghali, Opt. Mater. (2021). https://doi.org/10.1016/j.optmat.2021.111659